

Machine Learning Modeling of Temperature-Dependent Optoelectronic Properties of Anharmonic Solid Solutions

Pol Benítez,^{1,2,*} Cibrán López,^{1,2} Edgardo Saucedo,^{2,3} and Claudio Cazorla^{1,2,4,†}

¹*Department of Physics, Universitat Politècnica de Catalunya, 08019 Barcelona, Spain*

²*Research Center in Multiscale Science and Engineering, Universitat Politècnica de Catalunya, 08019 Barcelona, Spain*

³*Departament d'Enginyeria Electrònica, Universitat Politècnica de Catalunya, 08034 Barcelona, Spain*

⁴*Institució Catalana de Recerca i Estudis Avançats (ICREA), Passeig Lluís Companys 23, 08010 Barcelona, Spain*

Abstract. Leveraging strong optoelectronic responses to external stimuli, such as temperature and electric fields, is central to the development of advanced photonic technologies, including adaptive photodetectors and reconfigurable photovoltaic devices. However, only a limited number of semiconducting materials, typically characterized by strong electron–phonon coupling, are known to exhibit such pronounced responsiveness, and their equilibrium optoelectronic properties are often not optimally suited for targeted applications. Chemical engineering strategies, such as doping and solid-solution mixing, are therefore widely employed to fine-tune the electronic and optical properties of semiconductors. Predicting the impact of such modifications, however, remains highly challenging due to the intrinsic complexity of chemically disordered and anharmonic systems, as well as the computational limitations of conventional first-principles approaches. In this work, we introduce a new computational framework that combines *ab initio* electronic-structure methods with machine-learning techniques to achieve first-principles precision in the prediction of optoelectronic properties of anharmonic solid solutions at finite temperature. We apply this approach to $\text{Ag}_3\text{SBr}_x\text{I}_{1-x}$ solid solutions, an emergent class of optoelectronic materials that have been experimentally shown to exhibit large band-gap tunability and strong responses to thermal excitations. Our results provide quantitative insight into the interplay between chemical disorder, lattice dynamics, and electronic structure in these materials. More broadly, this study establishes a general strategy for the accurate modeling of optoelectronic functionality in chemically disordered semiconductors.

Keywords: electron-phonon coupling, anharmonicity, solid-solution modeling, graph neural networks, machine learning interatomic potentials

I. INTRODUCTION

Semiconducting materials play a central role in contemporary and emerging energy and optoelectronic technologies, including photovoltaics and integrated electronic circuits. Their functional behaviour is dictated by the electronic band structure, which in many systems is not a static quantity but evolves with temperature due to electron–phonon coupling and thermal expansion effects [1, 2]. Substantial thermal renormalisation of optoelectronic properties has been reported across a wide range of semiconductors, from molecular crystals [3] to inorganic materials [4, 5], highlighting the fundamental importance of finite-temperature effects in determining device-relevant properties.

An especially revealing class of materials in this context are strongly anharmonic perovskite-like systems, which can exhibit exceptionally large temperature-driven changes in their electronic structure. Among these, chalcogenide anti-perovskites (CAP) [6], exemplified by Ag_3SBr [7, 8], display giant band-gap reductions of approximately 20–60% at room temperature relative to

their zero-temperature values. Such behaviour arises from the pronounced anharmonicity of their lattice dynamics and the strong coupling between electronic and vibrational degrees of freedom. Beyond thermal stimuli, the combination of structural inversion symmetry and polar low-energy phonon modes in CAP has led to the proposal that external electric fields could be used to induce rapid and sizable optoelectronic changes [9], offering an alternative route to dynamically control of band gaps and light-absorption features.

Recent experimental work has further expanded the scope of CAP by demonstrating chemically synthesised solid solutions of the form $\text{Ag}_3\text{SBr}_{1-x}\text{I}_x$ with highly promising optoelectronic properties [10]. These materials combine narrow band gaps around 1.0 eV with strong absorption across the visible spectrum, while retaining considerable compositional flexibility through Br/I alloying. Their highly anharmonic lattice dynamics, temperature-dependent electronic structure, and coexistence of photoactivity with significant ionic mobility position CAP solid solutions as a particularly rich platform for exploring multifunctional behaviour in semiconductors. Together, these findings point to an unusually high degree of tunability in CAP optoelectronics and raise fundamental questions regarding the microscopic mechanisms governing their finite-temperature properties.

* pol.benitez@upc.edu

† claudio.cazorla@upc.edu

From a theoretical perspective, however, CAP present formidable challenges. Their strong anharmonicity renders conventional harmonic or quasi-harmonic descriptions inadequate, requiring an explicit treatment of electron–phonon coupling beyond these approximations, as well as thermal expansion effects [11]. While *ab initio* methods such as density functional theory (DFT) and *ab initio* molecular dynamics (AIMD) have successfully uncovered key aspects of CAP behaviour, they are computationally demanding and scale poorly with chemical disorder and reduced symmetry. As a result, the systematic modelling of CAP solid solutions, and, more broadly, of complex low-symmetry perovskite-inspired materials, remains largely out of reach, limiting both fundamental understanding and rational materials design.

In this study, we address this challenge by introducing a combined machine-learning (ML) and first-principles framework designed to efficiently capture anharmonic lattice dynamics and electron–phonon coupling in chemically disordered solids. We illustrate the capabilities of this approach on the technologically relevant $\text{Ag}_3\text{SBr}_x\text{I}_{1-x}$ system. By integrating machine-learning interatomic potentials (MLIP) [12, 13] with predictive graph neural networks (GNN) models [14] trained on DFT data, we achieve near first-principles accuracy for energies, forces, stresses, and band gaps at a fraction of the computational cost. This approach enables a systematic and physically transparent exploration of thermal effects on vibrational stability and optoelectronic properties in low-symmetry materials, providing a new theoretical pathway for understanding and ultimately controlling dynamically reconfigurable semiconductor functionalities.

II. RESULTS AND DISCUSSION

We focus on Ag-based chalcogenide anti-perovskite (CAP) solid solutions with general chemical formula $\text{Ag}_3\text{SBr}_x\text{I}_{1-x}$ (Fig. 1a). These materials can be synthesised via a variety of physical and chemical routes [7, 8, 10], making them experimentally accessible and well suited for systematic investigation. Parent CAP are characterised by a giant band-gap reduction with increasing temperature (Fig. 1b), a behaviour that originates from their pronounced lattice anharmonicity and strong electron–phonon coupling [6, 9]. This combination of properties makes CAP-based compounds a particularly compelling testbed for the solid-solution modelling formalism introduced in this work.

In addition to thermal effects, CAP are predicted to exhibit band-gap variations of comparable magnitude under the application of external electric fields (Fig. 1c). In this case, the underlying mechanism involves the condensation of polar phonon modes from the reference centrosymmetric cubic $Pm\bar{3}m$ phase (Fig. 1d), highlighting the intimate coupling between lattice dynamics and electronic struc-

ture. Here, we investigate $\text{Ag}_3\text{SBr}_x\text{I}_{1-x}$ solid solutions (Fig. 1e) by explicitly considering the stoichiometries $x \in \{0, 0.125, 0.25, 0.375, 0.5, 0.625, 0.75, 0.875, 1\}$.

A. General workflow

We begin by constructing a comprehensive DFT dataset for $\text{Ag}_3\text{SBr}_x\text{I}_{1-x}$ solid solutions using both semilocal (PBEsol [15]) and range-separated hybrid (HSEsol [16]) exchange–correlation functionals. Accurate prediction of temperature-dependent band gaps in strongly anharmonic materials requires explicit treatment of electron–phonon coupling [6, 9], which in practice entails sampling atomically displaced configurations representative of thermal fluctuations [17]. Accordingly, the dataset comprises total energies, atomic forces, stresses, and electronic band gaps evaluated on such thermally perturbed structures (additional details are provided in the following section).

While PBEsol enables efficient evaluation of structural and vibrational properties, its well-known self-interaction errors limit the reliability of band-gap predictions [18], thereby necessitating hybrid-functional accuracy. However, for chemically disordered solid solutions with large and low-symmetry simulation cells, direct hybrid-DFT calculations become computationally prohibitive. To overcome this limitation, we adopt a dual machine-learning strategy (Fig. 2). The PBEsol dataset is used to finetune a pre-trained universal MLIP [13], which is subsequently employed for ionic relaxations, chemical-disorder exploration, phonon dispersion calculations, and finite-temperature molecular dynamics (MD) simulations (Fig. 2a). In parallel, the HSEsol band-gap dataset is used to adjust a GNN model, initially trained on the PBEsol dataset, capable of reproducing hybrid-DFT band gaps with high fidelity (Fig. 2b and Methods). This blended approach enables the explicit treatment of chemical disorder, anharmonic lattice dynamics, and hybrid-level electronic properties within a computationally tractable framework.

The combination of the fine-tuned MLIP and accurate GNN model enables a unified workflow for evaluating finite-temperature band-gap renormalisation in CAP solid solutions (Fig. 2c). Starting from the cubic $Pm\bar{3}m$ antiperovskite unit cell, we construct supercells sufficiently large to accommodate each targeted stoichiometry x . Chemical disorder is then sampled using the MLIP. When the number of symmetry-inequivalent configurations for a given composition is manageable (considered here as $\lesssim 100$ due to computational affordability reasons), all configurations are retained for further analysis. For compositions with a much larger configurational space ($> 1,000$), about a hundred of representative structures are generated using a random sampling procedure; all the resulting configurations are subsequently relaxed using the MLIP, and ranked according to their equilibrium energies.

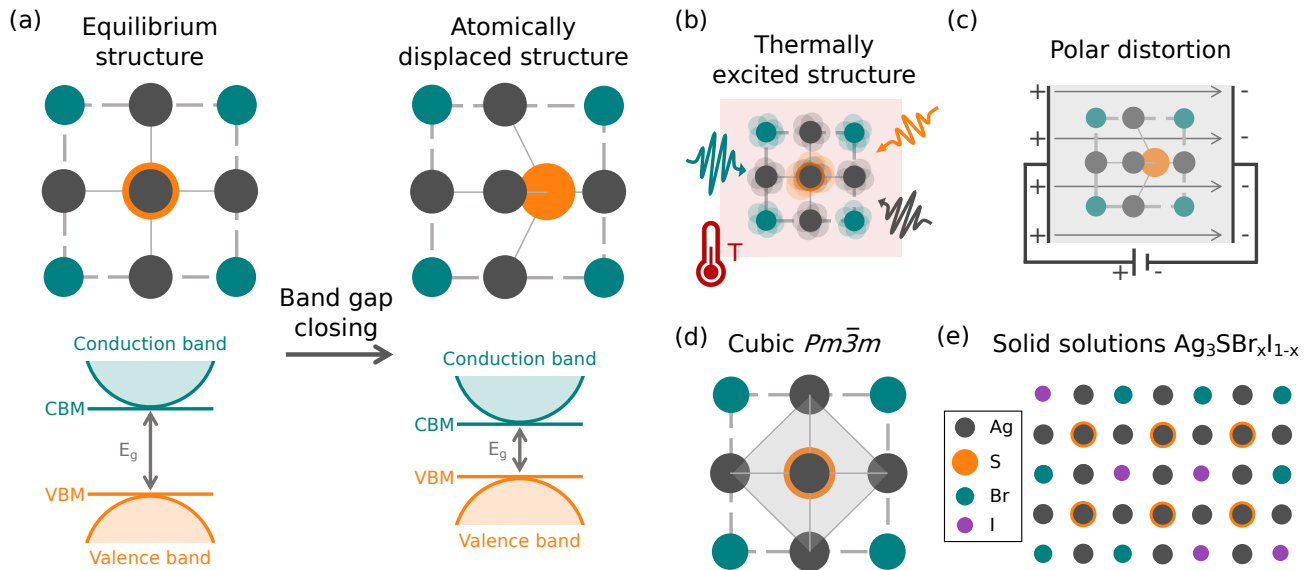


FIG. 1. **Band-gap response to external stimuli in CAP.** (a) Band-gap closing as a result of structural perturbations condensing in the equilibrium cubic CAP structure. Types of structural perturbations that may render band-gap closing in CAP, (b) general thermal fluctuations, and (c) a polar distortion stabilised by an electric field. (d) Cubic anti-perovskite structure of reference with space group $Pm\bar{3}m$. (e) CAP solid solutions with chemical formula $Ag_3SBr_xI_{1-x}$.

The relaxed lowest-energy configurations are subsequently assessed for vibrational stability by computing its phonon frequencies with the MLIP. Only vibrationally stable structures are retained for the final stage of the analysis, in which temperature-dependent band gaps are evaluated. Long MD simulations are performed at selected temperatures using the MLIP, and electronic band gaps are computed for statistically uncorrelated MD snapshots using the GNN model. The ensemble-averaged band gaps obtained in this manner (Methods, Fig. 2c) provide estimates of the temperature-renormalised band gaps of CAP solid solutions. In the following sections, we describe in detail the generation of the DFT datasets, the training of the GNN model, and the fine-tuning of the MLIP, together with a critical analysis of their performance.

B. Dataset generation

The datasets used for training the GNN band-gap model and for fine-tuning the MLIP were generated by introducing temperature-dependent phononic displacements, \mathbf{u}^{phon} , into the reference antiperovskite cubic $Pm\bar{3}m$ structure [17]. Phonon dispersions for the parent CAP compounds Ag_3SBr and Ag_3SI were computed using the small-displacement method as implemented in the **Phonopy** package [19, 20]. Atomic fluctuations about equilibrium positions were evaluated within the quasi-harmonic approximation [21–23] according to the expres-

sion:

$$u_{j,\alpha}^{\text{phon}} = \epsilon \cdot \zeta_{j,\alpha}$$

$$\zeta_{j,\alpha}^2 = \frac{\hbar}{2Nm_j} \sum_{\mathbf{q},\nu} \frac{1}{\omega_\nu(\mathbf{q})} (1 + 2n_\nu(\mathbf{q}, T)) |e_\nu^\alpha(j, \mathbf{q})|^2 \quad (1)$$

where \hbar is the reduced Planck constant, N is the total number of atoms in the unit cell, m_j is the atomic mass of atom j , \mathbf{q} denotes a reciprocal-space vector, α stands for Cartesian direction, ν is a phonon mode branch index, and ω_ν , n_ν , and e_ν correspond to the phonon frequency, Bose-Einstein occupation distribution, and phonon eigenvector, respectively. The prefactor ϵ is a random number sampled from the uniform distribution $\mathcal{U}[-1, 1]$, ensuring stochastic sampling of vibrational amplitudes.

All configurations were generated using a $2 \times 2 \times 2$ supercell containing 40 atoms. Chemical disorder was introduced through atomic substitutions consistent with the general formula $Ag_3SBr_xI_{1-x}$, including the limiting compositions $x = 0$ and $x = 1$. Phononic displacements were applied according to Eq. (1) for temperatures between 100 and 600 K. In addition, a small number of equilibrium configurations were included to ensure that the dataset retained explicit information on the ideal lattice geometry; these latter configurations were used in the GNN training but not in the MLIP fine-tuning.

For each displaced configuration, total energies, atomic forces, mechanical stresses, and electronic band gaps were computed using the semilocal PBEsol exchange-correlation functional [15], resulting in a total 2,200 configurations. A further 1,000 configurations were eval-

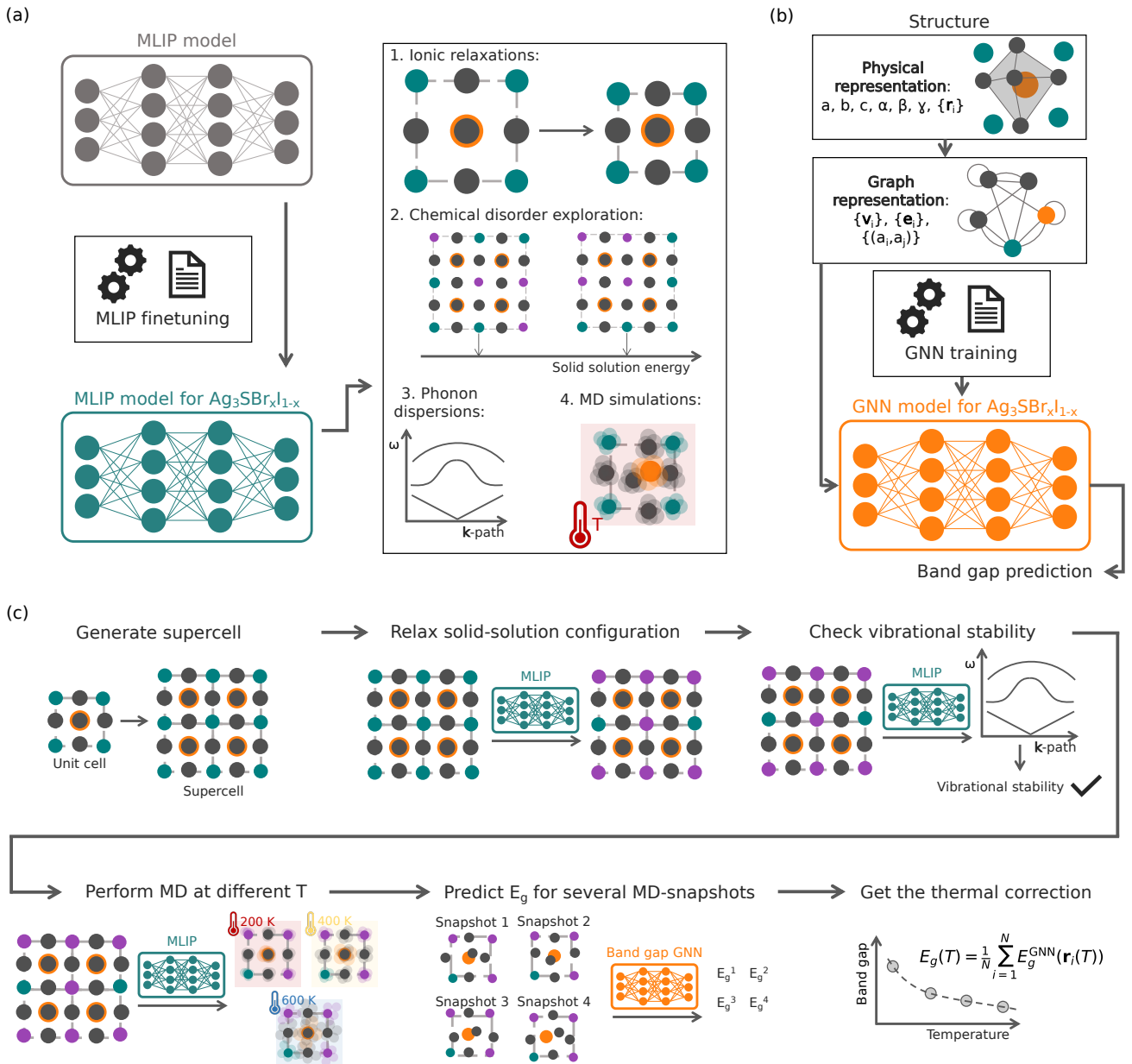


FIG. 2. **Computational workflow for predicting temperature-dependent band gaps in solid solutions.** (a) MLIP fine-tuning performed on a DFT-PBESol dataset of energies, forces and stresses. (b) Band-gap prediction workflow: the graph representation of a given atomic configuration is first obtained and subsequently processed by a GNN predictive model trained on a DFT-HSEsol dataset. (c) General workflow for accurate band-gap prediction in solid solutions, integrating thermal corrections.

uated using the range-separated hybrid HSEsol functional [16] to obtain high-accuracy band-gap data for re-training a GNN model (see next section).

C. GNN model

To ensure robust predictive performance of the GNN band-gap model, we carried out a systematic exploration of the hyperparameter space (Fig. 3a). This search in-

involved testing multiple GNN architectures and training parameters under a common validation protocol, ultimately identifying the optimal model configuration (see Methods and work [17] for technical details). As illustrated in Fig. 3a, the progressive refinement of model architectures converges toward a single “best model”, indicating that predictive performance is sensitive to architectural choices but stabilises once an adequate representational capacity is achieved.

The adopted architecture is schematically shown in

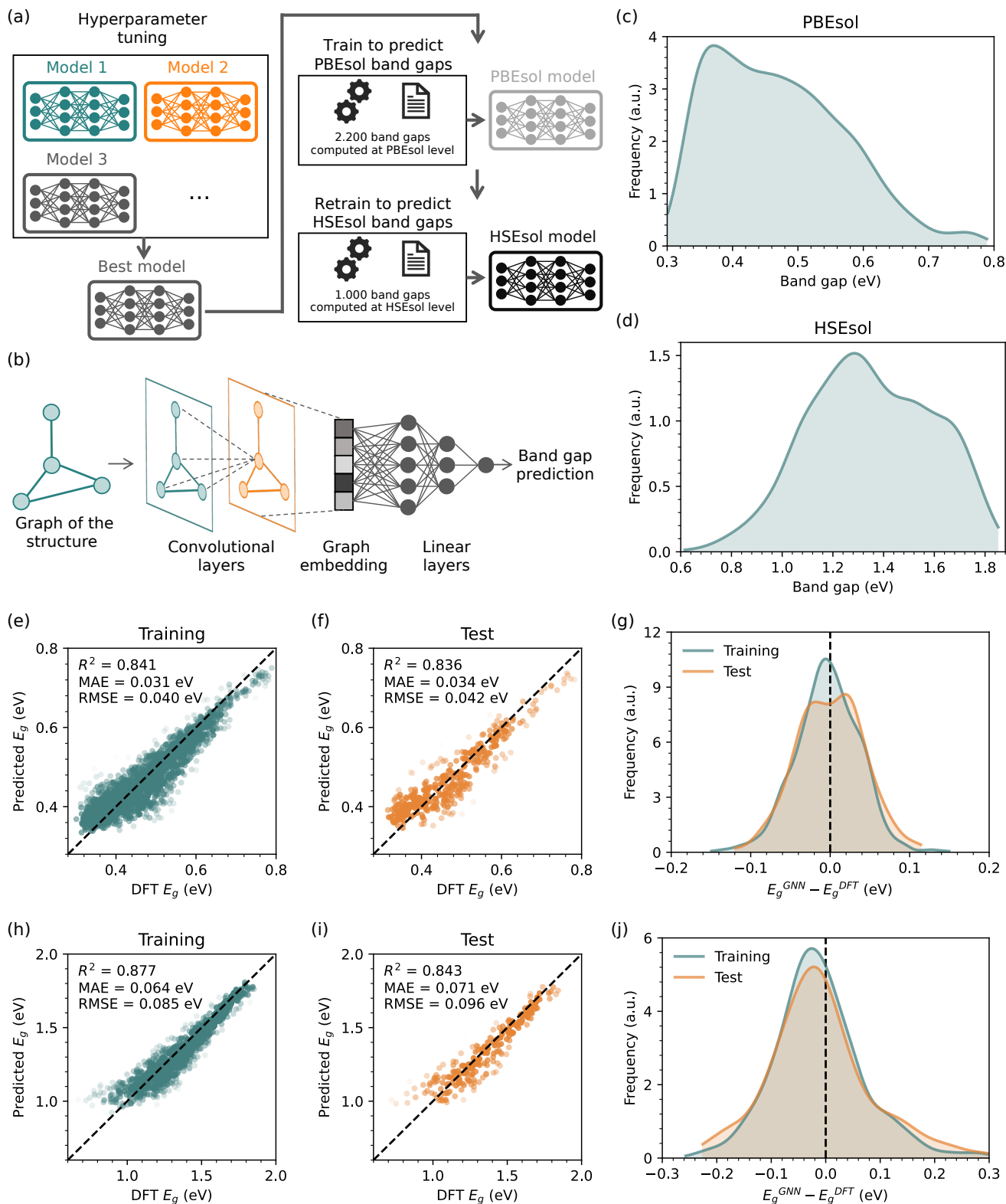


FIG. 3. **GNN training for accurate band-gap prediction.** (a) Workflow for training the GNN model on the DFT-HSEsol dataset. (b) GNN model architecture. (c,d) Band-gap distribution in the DFT-PBEsol and DFT-HSEsol training datasets. Predicted band gap vs. DFT calculated band gap for the training (e) and test (f) DFT-PBEsol datasets. Predicted band gap vs. DFT calculated band gap for the training (h) and test (i) DFT-HSEsol datasets. Band gap error distribution for GNN band-gap prediction on the DFT-PBEsol (g) and DFT-HSEsol (j) datasets.

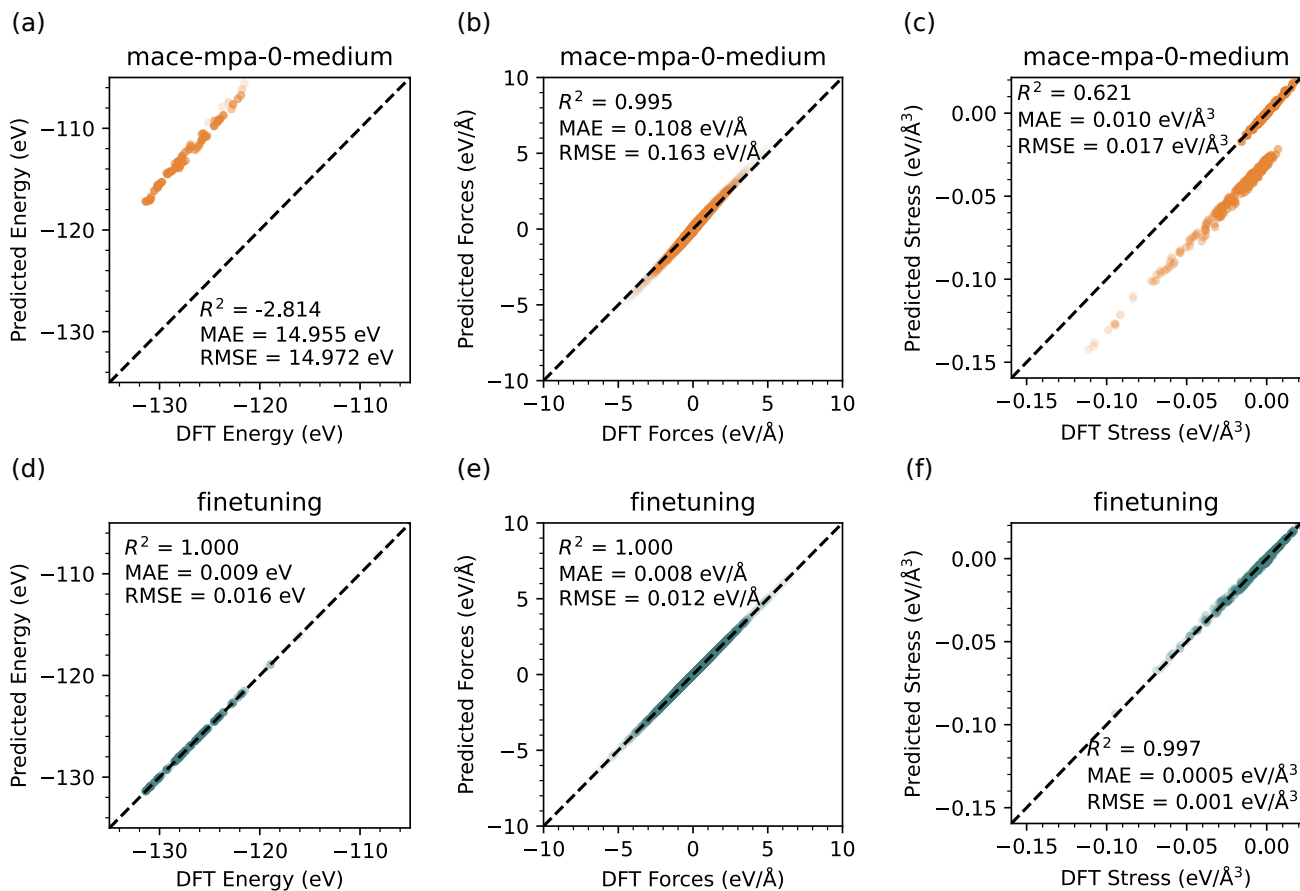


FIG. 4. **MLIP fine-tuning for CAP solid solutions.** DFT vs. MLIP prediction of (a) energies, (b) atomic forces, and (c) mechanical stress using the pre-trained MACE model [13], and (d-f) the fine-tuned MLIP.

Fig. 3b. The model operates on graph representations of the atomic structures, where nodes encode atomic species and local descriptors, and edges represent bonding environments. Through successive graph convolutional (message-passing) layers, node features are iteratively updated using information from neighbouring atoms weighted by edge attributes. This mechanism enables the model to learn how local chemical environments influence electronic structure. A global pooling operation then generates a fixed-size graph embedding, ensuring that structures with different numbers of atoms and bonds can be processed consistently. The embedding is subsequently passed through fully connected layers to produce a scalar output corresponding to the electronic band gap.

Training was performed in two sequential stages. The model was first trained on the larger PBEsol dataset and subsequently fine-tuned on the smaller HSEsol dataset (Sec. II B). The band-gap distributions for both datasets are shown in Figs. 3c and d. The PBEsol dataset exhibits a higher density of small band-gap values ($E_g \leq 0.6$ eV), reflecting the systematic band-gap underestimation of semilocal functionals. In contrast, the HSEsol dataset is shifted toward larger gap values, as expected for hybrid functionals. The separation between these distributions underscores the importance of the second training stage: it enables the model to correct for the intrinsic bias of semilocal DFT while retaining the structural diversity learned from the larger dataset. Importantly, the two datasets contain distinct atomic configurations, so the HSEsol fine-tuning step introduces genuinely new structural information rather than reusing previously seen geometries.

The performance of the model after the first and second training stages is summarised in Figs. 3e–g and h–j, respectively. The predicted versus DFT-computed band gaps for the training sets (Figs. 3e and h) and test sets (Figs. 3f and i) reveal a strong linear correlation, with only minor deviations at the extremes of the band-gap range. The error distributions (Figs. 3g and j) are narrowly centred around zero, indicating the absence of significant systematic bias. Notably, the second training stage preserves high predictive accuracy despite the smaller dataset size, demonstrating the effectiveness of the transfer-learning strategy from PBEsol to HSEsol data. In both cases, the model achieves test-set R^2 values above 0.8 and mean absolute errors (MAE) below 0.1 eV. Given that the intrinsic accuracy of DFT band-gap predictions is typically of the order of 0.1 eV, the GNN model therefore operates at near first-principles accuracy for $\text{Ag}_3\text{SBr}_x\text{I}_{1-x}$ solid solutions.

D. MLIP fine-tuning

As a foundational machine-learning interatomic potential (MLIP), we selected the MACE framework in the `mace-mpa-0-medium` flavour [13, 24, 25]. The

MACE model was subsequently fine-tuned on our PBEsol dataset comprising total energies, atomic forces, and stress tensors in order to achieve a quantitatively accurate description of CAP solid solutions (Methods). The predictive performances of the original and fine-tuned models are compared in Fig. 4.

Both models provide highly accurate atomic force predictions, with R^2 values close to unity (Figs. 4b,e), indicating that the pre-trained foundational model captures the local bonding physics reasonably well. However, fine-tuning leads to a clear quantitative improvement, reducing the mean absolute error (MAE) in forces to 0.008 eV/Å. More substantial gains are observed in the prediction of total energies and stress tensor components. The re-trained MLIP achieves MAE values of 0.009 eV for energies and 0.0005 eV/Å³ for stresses (Figs. 4d,f), demonstrating an accurate and internally consistent description of both structural and mechanical properties.

The apparently poor energy performance of the pre-trained model (Fig. 4a) is largely attributable to a systematic offset between DFT and MACE reference energies, likely originating from differences in the exchange–correlation functional used during pre-training relative to PBEsol [15]. Once this offset is corrected through fine-tuning, the energy predictions align closely with the DFT values. In contrast, the pre-trained model shows limited transferability in predicting mechanical stress, as reflected by a relatively modest $R^2 = 0.621$ and MAE of 0.010 eV/Å³ (Fig. 4c). This highlights the importance of system-specific re-training when accurate elastic and thermomechanical properties are required.

To further validate the physical reliability of the fine-tuned MLIP, we assessed its ability to reproduce zero-temperature phonon dispersions for Ag_3SBr and $\text{Ag}_3\text{SBr}_{0.5}\text{I}_{0.5}$ (Fig. 5). Although phonon frequencies were not explicitly included in the training dataset, accurate reproduction of DFT phonons is essential to justify the use of the MLIP for ionic relaxations and finite-temperature MD simulations. Figures 5a,d compare harmonic phonon dispersions obtained from DFT with those predicted by the pre-trained and fine-tuned MLIP models, while Figs. 5b,e and Figs. 5c,f provide direct frequency-by-frequency comparisons.

The pre-trained `mace-mpa-0-medium` model reproduces the overall qualitative features of the DFT phonon spectra, confirming that the foundational model captures the dominant interatomic interactions. Nevertheless, moderate frequency shifts are observed in both the low- and high-frequency regimes for Ag_3SBr and $\text{Ag}_3\text{SBr}_{0.5}\text{I}_{0.5}$ (Figs. 5a,d), indicating incomplete transferability to CAP chemistry. By contrast, the fine-tuned model yields phonon dispersions that are nearly indistinguishable from the DFT results, including an accurate description of imaginary branches associated with lattice instabilities. The direct comparisons in Figs. 5c,f show R^2 values close to unity and MAE values below 0.1 THz, demonstrating quantitative agreement across the full vibrational spectrum.

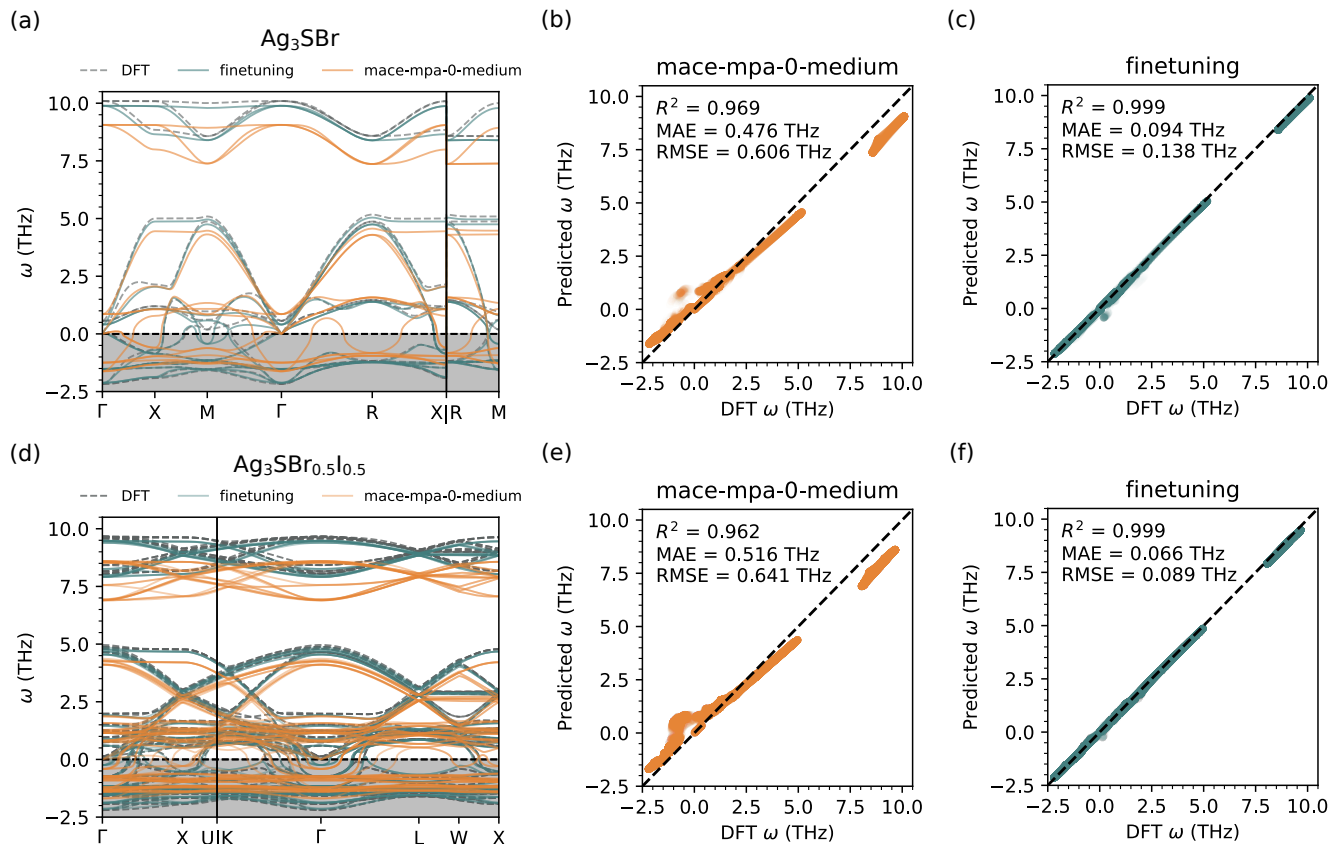


FIG. 5. **Finetuned MLIP tested on phonon dispersions.** (a) Phonon dispersions calculated for Ag_3SBr using DFT, a pre-trained MACE model [13], and the fine-tuned MLIP. MLIP predictions vs. DFT calculations for (b) a pre-trained MACE model, and (c) the fine-tuned MLIP. (d-f) Equivalent phonon results obtained for a $\text{Ag}_3\text{SBr}_{0.5}\text{I}_{0.5}$ solid solution.

Composition	E_g^{exp} (300 K)	E_g^{0K}	E_g^{300K}	E_g^{600K}
$x = 0.0$	0.9	1.6	1.0	1.0
$x = 0.3$	1.0	1.6	1.1	1.0
$x = 0.5$	1.0	1.7	1.1	1.0
$x = 0.7$	1.0	1.8	1.1	1.0
$x = 1.0$	1.0	1.8	1.1	1.0

TABLE I. **Calculated and experimentally measured band gaps for CAP solid solutions.** Experimental values are extracted from previous work [10]. Both the experimental and theoretical uncertainties approximately amount to 0.1 eV. Results are expressed in units of eV.

Taken together, these results confirm that fine-tuning the MACE foundational model on a modest but physically diverse PBEsol dataset yields a highly accurate and transferable MLIP. The model reliably reproduces structural energetics, mechanical stresses, and lattice dynamics, thereby providing a robust foundation for the large-scale relaxations and finite-temperature simulations re-

quired to investigate CAP solid solutions.

E. Temperature-dependent optoelectronic properties of CAP solid solutions

Having established the accuracy of both the fine-tuned MLIP and predictive GNN band-gap model, we proceed to investigate the optoelectronic properties of chemically disordered $\text{Ag}_3\text{SBr}_x\text{I}_{1-x}$ solid solutions with $x \in \{0, 0.125, 0.25, 0.375, 0.5, 0.625, 0.75, 0.875, 1\}$. To maintain computational affordability while preserving configurational diversity, we employ a 40-atom simulation cell constructed as a $2 \times 2 \times 2$ supercell of the cubic $Pm\bar{3}m$ unit cell. In this representation, Br/I substitutions occur over eight lattice sites, resulting in a manageable number of symmetry-inequivalent configurations. For example, at $x = 0.5$, a total of 70 distinct configurations arise, all of which can be explicitly simulated.

For each composition, all symmetry-inequivalent configurations were fully relaxed using the fine-tuned MLIP and ranked according to their equilibrium energies. The lowest-energy configuration at each stoichiometry was selected for subsequent lattice-dynamical analysis. Phonon

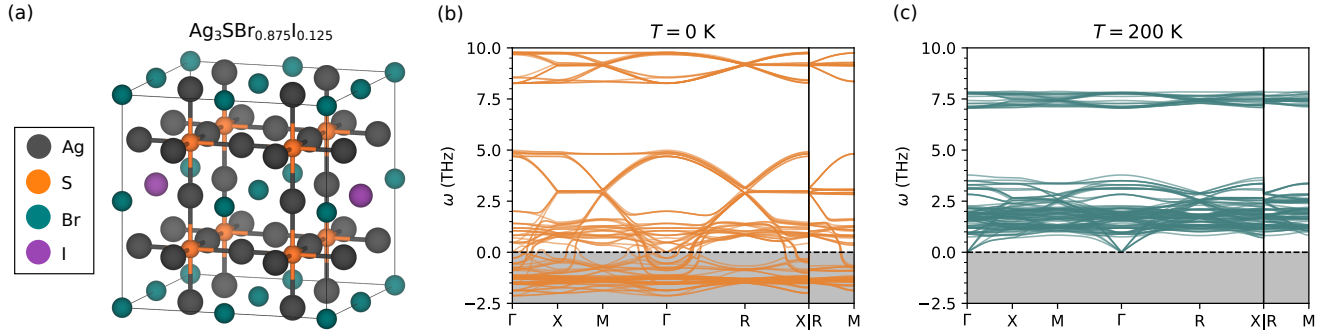


FIG. 6. **Solid solution vibrational stability.** (a) Representation of the equilibrium structure determined for $\text{Ag}_3\text{SBr}_{0.875}\text{I}_{0.125}$ with the fine-tuned MLIP model. Phonon dispersions calculated at (b) $T = 0 \text{ K}$, and (c) at $T = 200 \text{ K}$ with the fine-tuned MLIP model.

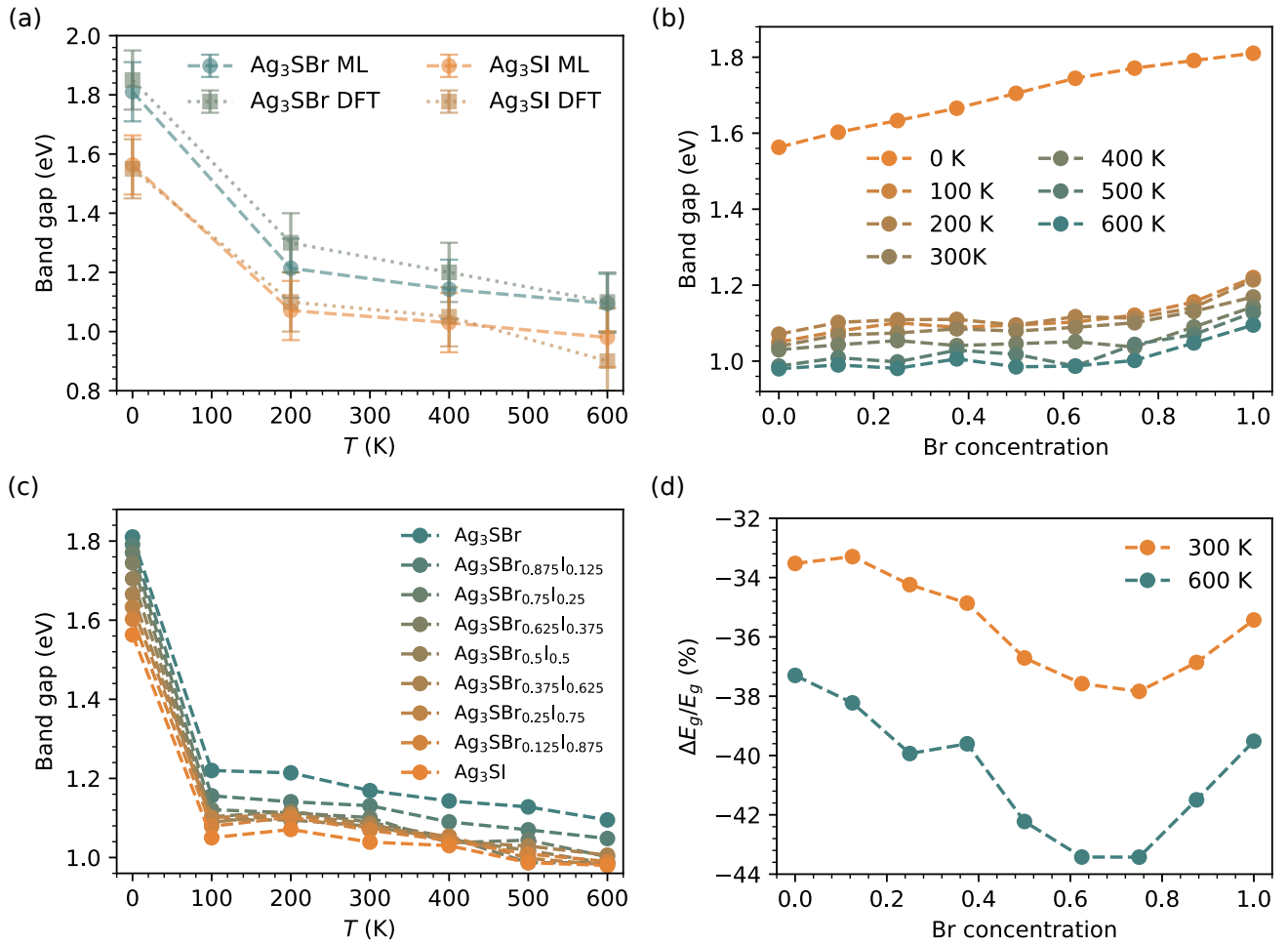


FIG. 7. **Temperature-renormalised band gaps of CAP solid solutions.** (a) T -dependent band gaps obtained for Ag_3SBr and Ag_3SI with the DFT-HSEsol method and with the ML-based approach introduced in this work. (b) Band gap of CAP solid solutions expressed as a function of Br concentration at different temperatures; error bars amount to 0.1 eV, not shown to avoid overcrowding. (c) Band gap of CAP solid solutions expressed as a function of temperature at different Br concentrations; error bars amount to 0.1 eV, not shown to avoid overcrowding. (d) Relative variation of the band gap with respect to $T = 0 \text{ K}$ as a function of Br concentration at two different temperatures.

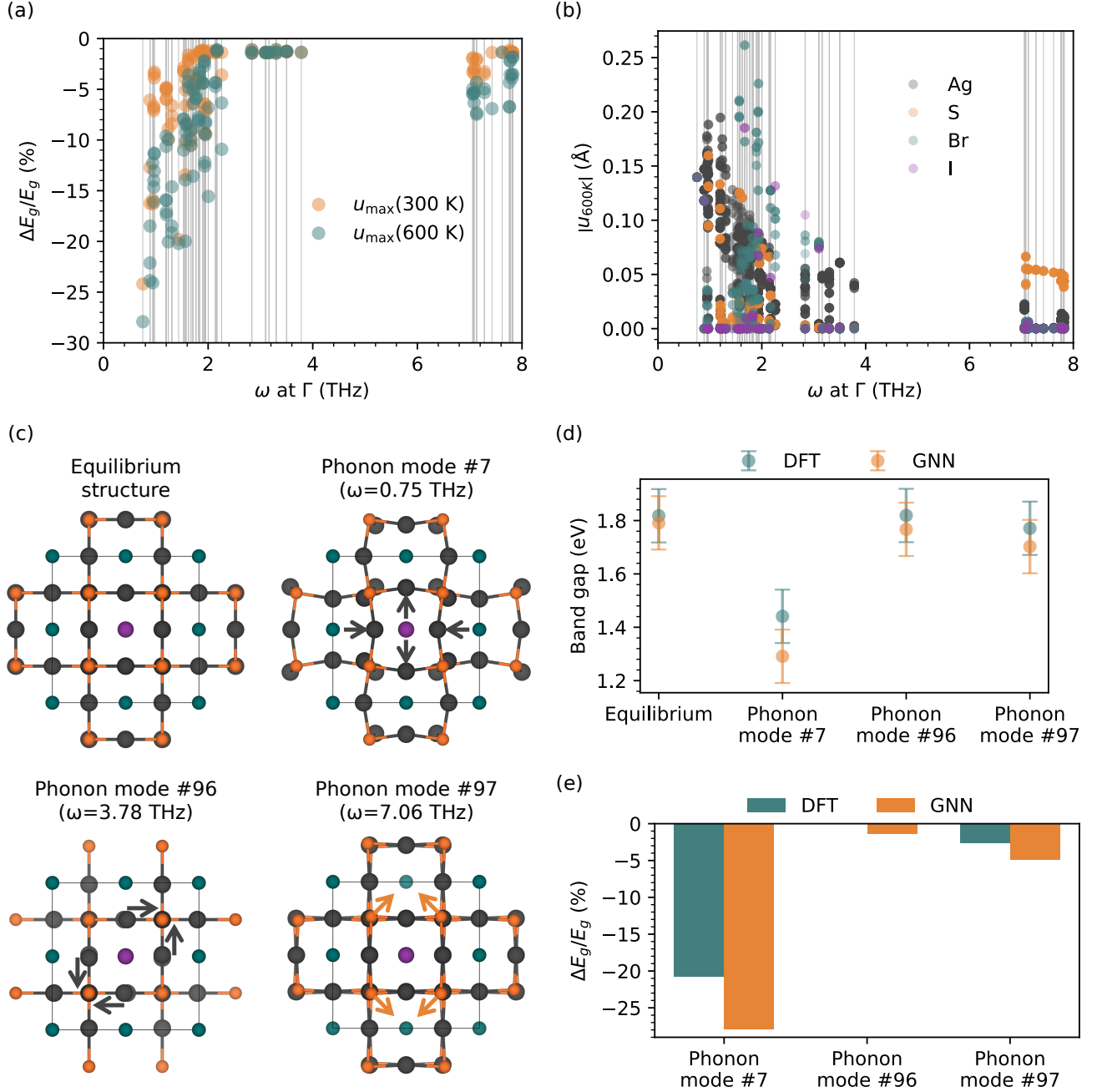


FIG. 8. **Electron-phonon coupling mechanisms in $\text{Ag}_3\text{SBr}_{0.875}\text{I}_{0.125}$.** (a) Relative band-gap variation under Γ -phonon mode atomic displacements at $T = 300$ and 600 K. (b) Atomic displacements corresponding to Γ -phonon modes calculated at $T = 600$ K. (c) Representation of the equilibrium structure and different Γ -phonon eigenmodes. Arrows indicate most relevant atomic displacements. (d) Comparison between the DFT calculated and GNN predicted band gaps for the four atomic configurations represented in (c). (e) Relative band-gap change with respect to the equilibrium structure for specific Γ -phonon distortions.

dispersion relations were computed both at $T = 0$ K and under finite-temperature conditions. This step is essential because CAP systems are strongly anharmonic, and their vibrational stability can depend sensitively on temperature [6, 9, 11]. Finite-temperature phonons were obtained using a normal-mode decomposition technique based on MD trajectories [26] (Methods), allowing anharmonic effects to be explicitly incorporated.

Figure 6 illustrates representative phonon dispersions for $\text{Ag}_3\text{SBr}_{0.875}\text{I}_{0.125}$, shown at $T = 0$ K (Fig. 6b) and at $T = 200$ K (Fig. 6c). At zero temperature, the presence of imaginary phonon branches indicates vibrational instability. Upon increasing temperature, however, these unstable modes are dynamically stabilised, and the spectrum becomes entirely real. This thermally induced stabilisation is consistent with previous findings for the parent compounds Ag_3SBr and Ag_3SI [6, 11]. Supplementary Figs. 1–6 demonstrate that analogous behaviour occurs across the full compositional range considered here, confirming that dynamic stabilisation is a general feature of $\text{Ag}_3\text{SBr}_x\text{I}_{1-x}$ solid solutions. These results further highlight the central role of anharmonicity in governing the structural stability of CAP materials.

After establishing vibrational stability at finite temperature, we evaluated the temperature renormalisation of the electronic band gap. As a first validation of our ML-based framework, we applied it to the parent compounds Ag_3SBr and Ag_3SI , for which accurate first-principles and experimental data are available [6]. The calculated band gaps at 0, 200, 400, and 600 K show excellent agreement, within the numerical uncertainties, with previous DFT-AIMD results [6] (Fig. 7a). Since those first-principles results are themselves in quantitative agreement with experiment [6] (Table 1), this comparison confirms that the present ML-driven approach retains first-principles accuracy while enabling significantly enhanced computational efficiency.

The temperature-renormalised band gaps for all investigated compositions are summarised in Figs. 7b,c as functions of both Br concentration and temperature. At zero temperature, the band gap increases systematically with increasing Br content (Fig. 7b), reflecting the intrinsic compositional tuning of the electronic structure. This overall trend persists at finite temperatures, although minor non-monotonic variations appear in the intermediate range $0.4 \leq x \leq 0.6$, suggesting a subtle interplay between chemical disorder and lattice dynamics.

For any fixed composition, the band gap decreases with increasing temperature, with the largest reductions occurring in the low-temperature regime (approximately $0 \leq T \leq 100$ K), where electron-phonon coupling effects are most pronounced (Figs. 7b,c). The relative band-gap changes with respect to the zero-temperature values are shown in Fig. 7d. Thermal renormalisation effects are maximal in the intermediate compositional range $x \approx 0.6$ – 0.8 , reaching approximately -38% and -44% at 300 and 600 K, respectively. In contrast, the smallest relative reductions are observed for the parent

compound Ag_3SI (approximately -33% and -37% at 300 and 600 K), although even these values remain remarkably large in absolute terms.

Table 1 presents a comparison between our finite-temperature band-gap predictions for CAP solid solutions and the available experimental data reported in work [10]. The estimated numerical uncertainties are on the order of 0.1 eV for both the experimental measurements and the calculations. When thermal effects are explicitly accounted for through the ML-based framework introduced in this work, the agreement between first-principles predictions and experiment is excellent across all investigated compositions, remaining fully within the corresponding error bars.

Overall, these results validate the accuracy, reliability, and robustness of our ML-enabled predictive framework for optoelectronic properties of solid solutions under realistic finite-temperature conditions. Furthermore, they demonstrate that chemical composition and temperature act as powerful and intrinsically coupled tuning parameters for controlling the optoelectronic response of CAP solid solutions. In this context, anharmonic lattice dynamics emerge as a key physical mechanism governing the interplay between structural disorder and electronic structure, thereby enabling fine evaluation of band-gap behavior.

F. Electron-phonon coupling mechanisms

In addition to evaluating finite-temperature band-gap renormalisation, we used our ML-based framework to analyse in greater detail the microscopic origin of electron-phonon coupling in CAP solid solutions. Specifically, we quantified the band-gap variations induced by frozen Γ -point phonon distortions of the reference antiperovskite structure, following a strategy analogous to that previously applied to the parent compounds Ag_3SBr and Ag_3SI [6, 9].

Figure 8a presents the relative band-gap change, referenced to the equilibrium value, computed at $T = 300$ and 600 K for $\text{Ag}_3\text{SBr}_{0.875}\text{I}_{0.125}$ under distortions corresponding to different Γ -phonon modes. The results are plotted as a function of the phonon frequency ω , while the associated atomic displacement patterns (evaluated at the highest temperature) are shown in Fig. 8b. A clear frequency-dependent trend emerges: the magnitude of the band-gap renormalisation roughly decreases with increasing phonon frequency, indicating that low-frequency modes contribute most strongly to the optoelectronic response.

The largest relative band-gap reductions, reaching approximately -30% , are concentrated in the low-frequency region ($\omega \leq 2$ THz), where the vibrational modes are dominated by Ag displacements (Fig. 8b). In contrast, modes in the intermediate frequency range (2.5–4.0 THz), characterised by coupled Ag and Br/I motions, produce negligible band-gap variations. At higher fre-

quencies ($\omega \geq 7$ THz), where S displacements dominate, moderate band-gap reductions of about -10% are observed. This hierarchy of contributions closely mirrors the behaviour previously reported for Ag_3SBr and Ag_3SI [9], reinforcing the conclusion that soft, Ag-dominated lattice vibrations play a central role in governing electron–phonon coupling in CAP materials.

To further validate the predictive accuracy of the GNN model, we performed explicit DFT calculations of band-gap variations induced by representative Γ -phonon distortions spanning the three frequency regimes identified above. The corresponding displacement patterns are illustrated in Fig. 8c, with arrows highlighting the dominant atomic contributions. As shown in Figs. 8d,e, the GNN predictions are in very good agreement with the DFT results, within numerical uncertainties.

Supplementary Figs. 7–12 present analogous $\Delta E_g/E_g$ calculations for the remaining compositions investigated in this work. Across all compositions, the same qualitative picture emerges: low-frequency modes induce the largest band-gap renormalisation, intermediate modes have diminished impact, and high-frequency modes produce moderate changes. These results provide a direct and quantitative link between lattice dynamics and optoelectronic response in CAP solid solutions. More broadly, the approach demonstrates how machine-learning models trained on first-principles data can be used not only to reproduce finite-temperature properties but also to dissect mode-resolved electron–phonon coupling in strongly anharmonic materials.

III. CONCLUSIONS

In this work, we have introduced and validated a machine-learning-assisted first-principles framework for the quantitative modelling of electron–phonon coupling and anharmonic lattice dynamics in chemically disordered solid solutions. By combining a fine-tuned MACE-based machine learning interatomic potential with a graph neural network trained to reproduce hybrid-DFT band gaps, we achieved near first-principles accuracy for energies, forces, stresses, phonon dispersions, and temperature-renormalised electronic band gaps in $\text{Ag}_3\text{SBr}_x\text{I}_{1-x}$ antiperovskites. The approach enables explicit sampling of chemical disorder, finite-temperature vibrational effects, and mode-resolved electron–phonon coupling at a computational cost that would be prohibitive within a fully hybrid-DFT framework.

Applied to $\text{Ag}_3\text{SBr}_x\text{I}_{1-x}$ solid solutions, our method reveals (i) systematic compositional tuning of the zero-temperature band gap, (ii) strong and composition-dependent thermal renormalisation reaching up to $\sim 40\text{--}45\%$ at elevated temperatures, and (iii) a dominant contribution of low-frequency, Ag-dominated vibrational modes to the electron–phonon coupling mechanism. We further demonstrate that these systems undergo temperature-induced dynamical stabilisation, con-

firmed the decisive role of anharmonic lattice effects in governing both structural and optoelectronic properties. The excellent agreement obtained with previous first-principles and experimental data for the parent compounds validates the quantitative robustness of the ML-driven strategy.

Beyond the specific case of CAP materials, the present formalism opens new perspectives for computational materials science. The methodology is directly transferable to other highly anharmonic and chemically complex systems, including hybrid halide perovskites, oxide and chalcogenide perovskites, thermoelectric materials, phase-change materials, and low-symmetry solid solutions used in photovoltaics and photocatalysis. In particular, it provides a practical route to investigate temperature-dependent band structures, vibrational stabilisation mechanisms, and mode-resolved electron–phonon interactions in systems where large supercells, chemical disorder, and hybrid-functional accuracy are simultaneously required.

More broadly, this work illustrates how machine learning can move beyond property interpolation and become a tool for physically interpretable modelling of coupled electronic and lattice degrees of freedom. By enabling systematic exploration of dynamically reconfigurable semiconductors, the framework paves the way for predictive design of materials whose optoelectronic response can be tuned through composition, temperature, strain, or external fields. We anticipate that such approaches will play an increasingly central role in addressing open problems related to anharmonicity-driven phase stability, thermal band-gap engineering, and multifunctional energy materials.

METHODS

DFT calculations

DFT calculations [27, 28] were performed with the VASP software [29–31] and semilocal PBEsol exchange–correlation functional [15] to calculate energies, atomic forces, mechanical stresses and band gaps. Wave functions were represented in a plane-wave basis set truncated at 550 eV. For reciprocal-space Brillouin zone sampling, we selected dense k-point grids equivalent to that of $12 \times 12 \times 12$ for the 5-atoms cubic antiperovskite unit cell. By using these parameters, we obtained zero-temperature energies converged to within 0.5 meV per formula unit. For geometry relaxations, a force tolerance of $0.005 \text{ eV \AA}^{-1}$ was imposed in all the atoms. Electronic density of states and accurate band gaps were computed with the range-separated hybrid HSEsol functional [16].

Graph generation

Graphs representing materials structures were generated by employing a radius cutoff method [32]. Each atom in the unit cell is represented as a node with four different chemical features: atomic number, atomic mass, atomic radius, and electronegativity. A cutoff radius R_{cutoff} defines the maximum distance between pairs of atoms to be considered. Pairs of atoms closer than R_{cutoff} , taken equal to 5.5 Å in this study, are connected by an edge with their Euclidean distance as the edge feature. Atoms not connected by edges can still *communicate* via the message passing implemented in the GNN architecture. The features of nodes and edges are all of them normalized to take values between 0 and 1. The structure periodicity is ensured by constructing a supercell large enough to contain all cutoff spheres centered on each unit cell atom. Connections between unit cell atoms and their periodic pictures in the supercell are represented in the graph as a self-edge. Further details in the graph construction workflow are provided in work [17].

GNN technical parameters

Graph Neural Networks (GNN) for band gap prediction were implemented using the PyTorch Geometric framework [33], which is built on top of the PyTorch machine learning library [14]. Different GNN architectures with different parameters were trained and we studied their performance on determining band gaps by doing a hyperparameter exploration. Further details in the hyperparameter study of different GNN architectures are provided in [17].

The architecture of the best GNN band-gap predicting model consists of a first convolutional layer that receives the four features of each node and generates 64 node features by using the edge feature, followed by a batch normalization and applying a ReLU activation function. A second convolutional layer is used receiving now 64 node features, followed again by a batch normalization and ReLU. Then a global max pooling is applied followed by a dropout of 40% of the features. The 64 features are then passed to a linear layer that outputs 16 features after applying a ReLU activation function. Finally, the 16 features are passed to a final linear layer that outputs a final feature after applying a sigmoid activation function. Band gaps are also normalized to be consistent with this last activation function.

MLIP fine-tuning details and calculations

As a foundational MLIP framework, we chose the higher order equivariant message passing model MACE [13, 24, 25]. Our antiperovskites dataset generated with the PBEsol functional was used to finetune MACE, with

95% of the structures grouped in the training set and 5% in the validation set. The parameters used for the re-training amount to a total of 256 equivariant messages, a distance cutoff of 8 Å, and an energy, atomic forces, and mechanical stress weights of 1, 150, and 10, respectively. To assess the performance of our fine-tuned model, we compare our results with those obtained with the pre-trained universal MACE model `mace-mpa-0-medium` [13].

The fine-tuned MLIP model was used to perform single point calculations (energy and atomic forces), ionic relaxations, and MD simulations. All these calculations were conducted within the Atomic Simulation Environment [34]. Ionic relaxations were performed by using the BFGS method with a convergence criterion of maximum force of 0.01 eV/Å. MD simulations were implemented by using a Langevin algorithm with a coefficient friction of 10^{-3} fs $^{-1}$, a time step of 1 fs, and a total simulation time of 50 ps. The velocities were initialized by a Maxwell-Boltzmann Distribution.

Anharmonic phonon calculations

The DynaPhopy software [35] was used to calculate the anharmonic lattice dynamics (i.e., T -renormalized phonons) of the studied systems. A normal-mode-decomposition technique [26] was employed in which the atomic velocities $\mathbf{v}_{jl}(t)$ (j and l represent particle and Cartesian direction indexes) generated during fixed-temperature MD simulation runs were expressed like:

$$\mathbf{v}_{jl}(t) = \frac{1}{\sqrt{Nm_j}} \sum_{\mathbf{q}s} \mathbf{e}_j(\mathbf{q}, s) e^{i\mathbf{q}\mathbf{R}_{jl}^0} v_{\mathbf{q}s}(t), \quad (2)$$

where N is the number of particles, m_j the mass of particle j , $\mathbf{e}_j(\mathbf{q}, s)$ a phonon mode eigenvector (\mathbf{q} and s stand for the wave vector and phonon branch), \mathbf{R}_{jl}^0 the equilibrium position of particle j , and $v_{\mathbf{q}s}$ the velocity of the corresponding phonon quasiparticle.

The Fourier transform of the autocorrelation function of $v_{\mathbf{q}s}$ was then calculated, yielding the power spectrum:

$$G_{\mathbf{q}s}(\omega) = 2 \int_{-\infty}^{\infty} \langle v_{\mathbf{q}s}^*(0) v_{\mathbf{q}s}(t) \rangle e^{i\omega t} dt. \quad (3)$$

Finally, this power spectrum was approximated by a Lorentzian function of the form:

$$G_{\mathbf{q}s}(\omega) \approx \frac{\langle |v_{\mathbf{q}s}|^2 \rangle}{\frac{1}{2} \gamma_{\mathbf{q}s} \pi \left[1 + \left(\frac{\omega - \omega_{\mathbf{q}s}}{\frac{1}{2} \gamma_{\mathbf{q}s}} \right)^2 \right]}, \quad (4)$$

from which a T -renormalized quasiparticle phonon frequency, $\omega_{\mathbf{q}s}(T)$, was determined as the peak position, and the corresponding phonon linewidth, $\gamma_{\mathbf{q}s}(T)$, as the full width at half maximum. These calculations were performed with the fine-tuned MACE model.

Thermal band-gap corrections

The electron-phonon correction to the band gap was computed as the difference between the band gap at zero temperature for the equilibrium structures and the average band gap obtained from the MD simulation at a given T [6, 9], that we can express with:

$$\Delta E_g(T) = \lim_{t_0 \rightarrow \infty} \int_0^{t_0} E_g^{\mathbf{R}(t)} dt - E_g(0), \quad (5)$$

where \mathbf{R} represents the positions of the atoms in the supercell at a given time t of the molecular dynamics simulation. This expression can be numerically approximated as:

$$\Delta E_g(T) = \frac{1}{N} \sum_{k=1}^N E_g(\{\mathbf{R}_k(T)\}) - E_g(0), \quad (6)$$

where the band gap is averaged over a finite number, N , of configurations.

Determination of the band gap was performed by using the GNN trained model on the HSEsol dataset for $\text{Ag}_3\text{SBr}_x\text{I}_{1-x}$ solid solutions. The MD simulations from which the atomic configurations were extracted were performed with the fine-tuned-MACE model.

SUPPORTING INFORMATION

Structural representation and phonon dispersions of all solid solutions investigated in this study; effect

of Γ -phonon displacements on the band gap for all solid solutions; estimation of coercive electric fields for inducing phonon distortions.

DATA AVAILABILITY

All relevant scripts, including model training workflows and data preprocessing routines, are freely accessible in the GitHub repository: <https://github.com/polbeni/ML-thermal-optoelectronics>.

ACKNOWLEDGMENTS

P.B. acknowledges support from the predoctoral program AGAUR-FI ajuts (2024 FI-1 00070) Joan Oró, which is backed by the Secretariat of Universities and Research of the Department of Research and Universities of the Generalitat of Catalonia, as well as the European Social Plus Fund. C.C. acknowledges support by MICIN/AEI/10.13039/501100011033 under the grants PID2023-146623NB-I00 and PID2023-147469NB-C21 and by the Generalitat de Catalunya under the grants 2021SGR-00343, 2021SGR-01519 and 2021SGR-01411. Computational support was provided by the Red Española de Supercomputación under the grants FI-2025-1-0015, FI-2025-2-0006, FI-2025-2-0028 and FI-2025-3-0004. This work is part of the Maria de Maeztu Units of Excellence Programme CEX2023-001300-M funded by MCIN/AEI (10.13039/501100011033).

-
- [1] Feliciano Giustino. Electron-phonon interactions from first principles. *Reviews of Modern Physics*, 89(1):015003, 2017.
 - [2] Kevin J Malloy and James A Van Vechten. Thermal expansion contributions to band gap and band offset temperature dependencies. *Journal of Vacuum Science & Technology B: Microelectronics and Nanometer Structures Processing, Measurement, and Phenomena*, 9(4):2212–2218, 1991.
 - [3] Bartomeu Monserrat, Edgar A Engel, and Richard J Needs. Giant electron-phonon interactions in molecular crystals and the importance of non-quadratic coupling. *arXiv preprint arXiv:1510.07904*, 2015.
 - [4] Bartomeu Monserrat, Ji-Sang Park, Sunghyun Kim, and Aron Walsh. Role of electron-phonon coupling and thermal expansion on band gaps, carrier mobility, and interfacial offsets in kesterite thin-film solar cells. *Applied Physics Letters*, 112(19), 2018.
 - [5] Yun Liu, Bartomeu Monserrat, and Julia Wiktor. Strong electron-phonon coupling and bipolarons in sb_2s_3 . *Physical Review Materials*, 7(8):085401, 2023.
 - [6] Pol Benítez, Siyu Chen, Ruoshi Jiang, Cibrán López, Josep-Lluís Tamarit, Jorge Íñiguez-González, Edgardo Saucedo, Bartomeu Monserrat, and Claudio Cazorla. Giant thermally induced band-gap renormalization in anharmonic silver chalcogenide antiperovskites. *Journal of Materials Chemistry C*, 13(20):10399–10412, 2025.
 - [7] Paz Sebastiá-Luna, Nathan Rodkey, Adeem Saeed Mirza, Sigurd Mertens, Snigdha Lal, Axel Melchor Gaona Carranza, Joaquín Calbo, Marcello Righetto, Michele Sessolo, Laura M. Herz, Koen Vandewal, Enrique Ortí, Mónica Morales-Masis, Henk J. Bolink, and Francisco Palazon. Chalcogenide antiperovskite thin films with visible light absorption and high charge-carrier mobility processed by solvent-free and low-temperature methods. *Chemistry of Materials*, 35(16):6482–6490, 2023.
 - [8] Francisco Palazon. Metal chalcogenides: Next generation photovoltaic materials? *Solar RRL*, 6(2):2100829, 2022.
 - [9] Pol Benítez, Ruoshi Jiang, Siyu Chen, Cibrán López, Josep-Lluís Tamarit, Edgardo Saucedo, Bartomeu Monserrat, and Claudio Cazorla. Band-gap tunability in anharmonic perovskite-like semiconductors driven by polar electron-phonon coupling. *Journal of the American*

- Chemical Society*, 147(41):37506–37520, 2025.
- [10] Ivan Caño, Jonathan W Turnley, Pol Benítez, Cibrán López-Álvarez, José-Miguel Asensi, David Payno, Joaquim Puigdollers, Marcel Placidi, Claudio Cazorla, Rakesh Agrawal, et al. Novel synthesis of semiconductor chalcogenide anti-perovskites by low-temperature molecular precursor ink deposition methodologies. *Journal of Materials Chemistry C*, 12(9):3154–3163, 2024.
- [11] Pol Benítez, Cibrán López, Cong Liu, Ivan Caño, Josep-Lluís Tamarit, Edgardo Saucedo, and Claudio Cazorla. Crystal structure prediction and phase stability in highly anharmonic silver-based chalcogenide antiperovskites. *PRX Energy*, 4(2):023002, 2025.
- [12] Ryan Jacobs, Dane Morgan, Siamak Attarian, Jun Meng, Chen Shen, Zhenghao Wu, Clare Yijia Xie, Julia H Yang, Nongnuch Artrith, Ben Blaiszik, et al. A practical guide to machine learning interatomic potentials—status and future. *Current Opinion in Solid State and Materials Science*, 35:101214, 2025.
- [13] Ilyes Batatia, David Peter Kovacs, Gregor N. C. Simm, Christoph Ortner, and Gabor Csanyi. MACE: Higher order equivariant message passing neural networks for fast and accurate force fields. In Alice H. Oh, Alekh Agarwal, Danielle Belgrave, and Kyunghyun Cho, editors, *Advances in Neural Information Processing Systems*, 2022.
- [14] Adam Paszke, Sam Gross, Francisco Massa, Adam Lerer, James Bradbury, Gregory Chanan, Trevor Killeen, Zeming Lin, Natalia Gimelshein, Luca Antiga, et al. Pytorch: An imperative style, high-performance deep learning library. *Advances in neural information processing systems*, 32, 2019.
- [15] John P Perdew, Adrienn Ruzsinszky, Gábor I Csonka, Oleg A Vydrov, Gustavo E Scuseria, Lucian A Constantin, Xiaolan Zhou, and Kieron Burke. Restoring the density-gradient expansion for exchange in solids and surfaces. *Physical review letters*, 100(13):136406, 2008.
- [16] Laurids Schimka, Judith Harl, and Georg Kresse. Improved hybrid functional for solids: The hsesol functional. *The Journal of Chemical Physics*, 134(2), 2011.
- [17] Pol Benítez, Cibrán López, Edgardo Saucedo, Teruyasu Mizoguchi, and Claudio Cazorla. Why physics still matters: Improving machine learning prediction of material properties with phonon-informed datasets. *arXiv preprint arXiv:2511.15222*, 2025.
- [18] Alejandro J Garza and Gustavo E Scuseria. Predicting band gaps with hybrid density functionals. *The journal of physical chemistry letters*, 7(20):4165–4170, 2016.
- [19] Atsushi Togo, Laurent Chaput, Terumasa Tadano, and Isao Tanaka. Implementation strategies in phono3py and phono3py. *J. Phys. Condens. Matter*, 35(35):353001, 2023.
- [20] Atsushi Togo. First-principles phonon calculations with phono3py and phono3py. *J. Phys. Soc. Jpn.*, 92(1):012001, 2023.
- [21] Riccardo Rurali, Carlos Escorihuela-Sayalero, Josep Lluís Tamarit, Jorge Íñiguez González, and Claudio Cazorla. Giant photocaloric effects across a vast temperature range in ferroelectric perovskites. *Phys. Rev. Lett.*, 133:116401, 2024.
- [22] Claudio Cazorla and Riccardo Rurali. Dynamical tuning of the thermal conductivity via magnetophononic effects. *Phys. Rev. B*, 105:104401, 2022.
- [23] C. Cazorla, D. Errandonea, and E. Sola. High-pressure phases, vibrational properties, and electronic structure of Ne(He)₂ and Ar(He)₂: A first-principles study. *Phys. Rev. B*, 80:064105, 2009.
- [24] Ilyes Batatia, Simon Batzner, Dávid Péter Kovács, Albert Musaelian, Gregor N. C. Simm, Ralf Drautz, Christoph Ortner, Boris Kozinsky, and Gábor Csányi. The design space of e(3)-equivariant atom-centered interatomic potentials, 2022.
- [25] Ilyes Batatia, Philipp Benner, Yuan Chiang, Alin M Elena, Dávid P Kovács, Janosh Riebesell, Xavier R Advincula, Mark Asta, Matthew Avaylon, William J Baldwin, et al. A foundation model for atomistic materials chemistry. *The Journal of chemical physics*, 163(18), 2025.
- [26] Tao Sun, Dong-Bo Zhang, and Renata M Wentzcovitch. Dynamic stabilization of cubic CaSiO₃ perovskite at high temperatures and pressures from ab initio molecular dynamics. *Physical Review B*, 89(9):094109, 2014.
- [27] Claudio Cazorla and Jordi Boronat. Simulation and understanding of atomic and molecular quantum crystals. *Reviews of Modern Physics*, 89(3):035003, 2017.
- [28] Peter E Blöchl. Projector augmented-wave method. *Physical review B*, 50(24):17953, 1994.
- [29] Georg Kresse and Jürgen Hafner. Ab initio molecular dynamics for liquid metals. *Physical review B*, 47(1):558, 1993.
- [30] Georg Kresse and Jürgen Furthmüller. Efficiency of ab-initio total energy calculations for metals and semiconductors using a plane-wave basis set. *Computational materials science*, 6(1):15–50, 1996.
- [31] Georg Kresse and Jürgen Furthmüller. Efficient iterative schemes for ab initio total-energy calculations using a plane-wave basis set. *Physical review B*, 54(16):11169, 1996.
- [32] Victor Fung, Jiaxin Zhang, Eric Juarez, and Bobby G Sumpter. Benchmarking graph neural networks for materials chemistry. *npj Computational Materials*, 7(1):84, 2021.
- [33] Matthias Fey and Jan Eric Lenssen. Fast graph representation learning with pytorch geometric. *arXiv preprint arXiv:1903.02428*, 2019.
- [34] Ask Hjorth Larsen, Jens Jørgen Mortensen, Jakob Blomqvist, Ivano E Castelli, Rune Christensen, Marcin Dułak, Jesper Friis, Michael N Groves, Bjørk Hammer, Cory Hargus, Eric D Hermes, Paul C Jennings, Peter Bjerre Jensen, James Kermode, John R Kitchin, Esben Leonhard Kolsbjerg, Joseph Kubal, Kristen Kaasbjerg, Steen Lysgaard, Jón Bergmann Maronsson, Tristan Maxson, Thomas Olsen, Lars Pastewka, Andrew Peterson, Carsten Rostgaard, Jakob Schiøtz, Ole Schütt, Mikkel Strange, Kristian S Thygesen, Tejs Vegge, Lasse Vilhelmsen, Michael Walter, Zhenhua Zeng, and Karsten W Jacobsen. The atomic simulation environment—a python library for working with atoms. *Journal of Physics: Condensed Matter*, 29(27):273002, 2017.
- [35] Abel Carreras, Atsushi Togo, and Isao Tanaka. DynaPhoPy: A code for extracting phonon quasiparticles from molecular dynamics simulations. *Computer Physics Communications*, 221:221–234, 2017.